WILEY | Hindawi

Research Article

Origin and Role of Kaolinization in Roll-Front Uranium Deposits and Its Response to Ore-Forming Fluids in the Yili Basin, China

Z. Y. Liu [iD],[1,2] S. P. Peng [iD],[1] M. K. Qin,[2] H. X. Liu,[2] Y. Y. Geng,[2] X. Zhang,[2] B. Ding,[2] and X. Q. Xiu[2]

[1]*State Key Laboratory of Coal Resources and Safe Mining, China University of Mining and Technology (Beijing), Beijing 100083, China*
[2]*Beijing Research Institute of Uranium Geology, China National Nuclear Corporation (CNNC), Beijing 100029, China*

Correspondence should be addressed to S. P. Peng; psp@cumtb.edu.cn

Kaolinite is a common mineral found in most Chinese sandstone-hosted uranium deposits. It occurs particularly in coal-bearing clastic rocks in northwest China, such as the uranium deposits in the Yili Basin, which is well known for hosting several large-scale roll-front uranium deposits. Previous studies have provided limited information on the origin of kaolinization and its role in the uranium mineralization. This study uses gas hydrocarbon, fluid inclusions, O and H isotope analysis, and scanning electron microscopy observations to investigate the formation of kaolinite in ore-hosting rocks from the Mengqiguer uranium deposit in the southern margin of the Yili Basin and to determine its role in the uranium mineralization. Results suggest that kaolinization is intense in the coal- and ore-bearing clastic rocks and that it is related to leaching of feldspar by acidic fluids. Vermicular kaolinite was formed by hydrocarbon-bearing fluid generated from coal and carbonaceous mudstone during a shallow-burial diagenetic stage at low homogenization temperatures ranging from 69 to 78°C and at relatively high salinities of 7.6–11.0 wt% $NaCl_{eq}$. Consequently, silicate minerals (such as feldspar) were leached and created secondary pores that hosted the subsequently formed uranium minerals. In contrast, micritic kaolinite was formed by infiltration of meteoric fluid enriched in U and O_2 at low homogenization temperatures of 51–63°C and low salinities of 1.2–3.7 wt% $NaCl_{eq}$. U^{6+} was sorbed by the micritic kaolinite through cation exchange, forming a U-bearing kaolinite complex; it was also reduced by pyrite and carbon detrital, thereby precipitating at the acidic oxidation front. The results of this study confirm that intense kaolinization is closely related to uranium mineralization in coal-bearing clastic rocks.

1. Introduction

Kaolinite is one of the most common and significant diagenetic minerals, and its formation is controlled by the composition of the material source and detritus, pH, temperature, pore water, and sealing or opening of the diagenetic system [1, 2]. The relation between pore water and diagenetic kaolinite morphology in sandstones from different depositional environments was studied by Irwin and Hurst [3]. According to their model, meteoric water flux results in the rapid generation of "nutrient" ions (Al^{3+}, Si^{4+}) for kaolinization through the dissolution of unstable detrital grains, such as feldspar and mica; the consequent rapid

kaolinite growth then affects the texture of these minerals. However, in the absence of meteoric water flux, such as in shale-enclosed marine sandstone, kaolinite growth proceeds slowly and produces fine-grained euhedral aggregate [4–8]. It has also been found that the formation of kaolinite in sandstones is related to migration of acidic fluids after, or during, diagenesis; for example, hydrocarbon-rich fluids in sandstones dissolve feldspar grains and produce kaolinite [9–13]. The variety of kaolinite in sandstone is nearly always well-crystallized, and it often occurs in vermicules and as discrete aggregates. Morphological and particle size variations in such kaolinite, and their textural relationships with other sandstone components, have been used as indicators to identify

whether they are authigenic [14]. In addition, the various morphologies of kaolinite and its distribution in sandstones suggest an interaction between pore water composition and detrital minerals.

According to the typical model of alteration and distribution of minerals in roll-front uranium deposits established by Harshman and Adams [15] and DeVoto [16], the kaolinite-rich zone, known as the "white bleaching zone" [17, 18], is formed at the limonitic front and is closely associated with uranium mineralization; therefore, it is an effective prospecting indicator for sandstone-hosted uranium deposits [15, 19, 20]. It has been verified that kaolinization in sandstone-hosted uranium deposits resulted from either local organic matter (OM) or foreign organic matter [21], and it is particularly related to liquid or gaseous OM, such as humic acid and hydrocarbon-aqueous species.

One of the most important roles of kaolinite in the uranium mineralization is its sorption of uranyl aqueous-species. This effect has been experimentally examined in great detail with respect to the types of sorption complexes, changes in pH and the ionic strength of the electrolyte solution, and concentrations of U [22–30]. Dong et al. [28] studied the sorption of uranyl species onto kaolinite and goethite, two of the most dominant minerals in sandstone-hosted uranium deposits, and showed that kaolinite was a stronger sorbent than goethite at pH < 4. This strong sorption capacity can be interpreted as being attributed in part to the ion exchange sites of kaolinite, which enable strong sorption of certain metal ions (e.g., UO_2^{2+}, Cu^{2+}, and Pb^{2+}) at low pH conditions.

Although kaolinization is widely found in sandstone-hosted uranium deposits, and it plays an important role in uranium sorption, few studies have focused on the origin of kaolinization and its role in the uranium mineralization. Kaolinite is a common mineral in most Chinese sandstone-hosted uranium deposits, particularly in the coal-bearing clastic rocks of northwest China. The deeply buried (>500 m) high-grade Mengqiguer uranium deposit is a typical roll-front uranium deposit hosed in the coal-bearing clastic rocks in the southern margin of the Yili Basin in northwest China. It contains an estimated resource of more than 10000 tU within an area of approximately 30 km^2, and an average uranium grade of 0.6%, which is much higher than the medium grade (0.05–0.4%) of this type [31].

The main focus of this study is to determine the association between kaolinization and uranium mineralization in the Mengqiguer uranium deposit. In addition, the origin of kaolinite and its response to ore-forming fluids are investigated using X-ray diffraction (XRD), SEM, gas hydrocarbon analysis, fluid inclusions, and O and H isotopes.

2. Geological Setting

The Yili Basin is a composite intermontane basin that was formed on a micromassif during the Tianshan orogen. The Yili block is often considered to be a part of the Central Tianshan microcontinent, which has a Proterozoic basement extending westward into Kazakhstan and Kyrgyzstan [33, 34]. The block is triangular and bordered by two late Paleozoic

suture zones: the North Tianshan Suture to the north and the Central Tianshan Suture to the south. Both suture zones were reworked by Permian postorogenic wrench faults, namely, the North Tianshan Fault (NTF) and the Nalati Fault (NF) (Figure 1(a), Liu et al. [35]). Overall, the western part of the southern margin of the Yili Basin shows weak tectonic activity and consists of a series of gentle anticlines and synclines, forming a gently dipping north monoclinic structure (basin slope). In contrast, the eastern part shows evidence of stronger tectonic activity and consists of complex asymmetrical synclines and anticlines. The middle part, consisting of the Zakisitan syncline, is a tectonic transition zone where tectonic activity is strong enough to invert or upturn sedimentary strata in the basin margin.

A series of roll-front uranium deposits have been discovered in the southern margin of the Yili Basin (Figure 1(b)). The Mengqiguer uranium deposit is located in the transition zone of Zakisitan syncline, which is an incomplete box fold with east–west–south side-flanks tilting to the northeast, and a synclinal axis dipping to the northeast. One of the probable uranium sources for the deposit are the acidic volcanic rocks, pyroclastic rocks, and granite of the Carboniferous–Permian age, which are exposed in the ranges of southern provenance. The average uranium content of these rocks is 6.2–12.9 ppm [36], and it is considered that uranium was leached and transported to the basin by oxygen-rich groundwater during weathering and erosion. Other probable contributors to the uranium source are the primary gray sandbodies and gray mudstones in the ore-hosting strata, which contain 6–10 ppm and 7–16 ppm uranium, respectively. Furthermore, the spring water in the southern source region and sedimentary terrains contains anomalous uranium concentrations of up to 9 ppb and 100 ppb, respectively, which also supports hypotheses that the uranium for ore formation could be derived from either one of these sources.

The sedimentary strata within the mining area belong to the Lower Jurassic Badaowan Formation (J_1b), Lower Jurassic Sangonghe Formation (J_1s), Middle Jurassic Xishanyao Formation (J_2x), Middle Jurassic Toutunhe Formation (J_2t), Cretaceous, and Neogene strata. The target ore-bearing strata for exploration are Middle–Lower Jurassic in age and include the lower member of the Sangonghe Formation (J_1s^1), upper member of the Sangonghe Formation (J_1s^2), lower member of the Xishanyao Formation (J_2x^1), and the upper member of the Xishanyao Formation (J_2x^3). The target strata were deposited during multiple sedimentary cycles with a fluvial positive rhythm, and they represent braided river delta sediments that formed coal–sand–coal stacks (Figure 2). The sandbodies between two coal seams are rich in carbon debris and pyrite, with an organic carbon content ranging from 0.11% to 1.93%, and carbon debris and numerous pyrite assemblage are dispersed in the sandstone cement. The host massive rocks have an argillaceous matrix and consist of conglomerate, sandy conglomerate, sandstone, and 10–18% gravel.

The uranium orebodies are tabular, lenticular, and roll-shaped (Figure 2). Tabular orebodies generally occur in the flanks of the interlayer oxidation zone, which are located
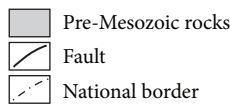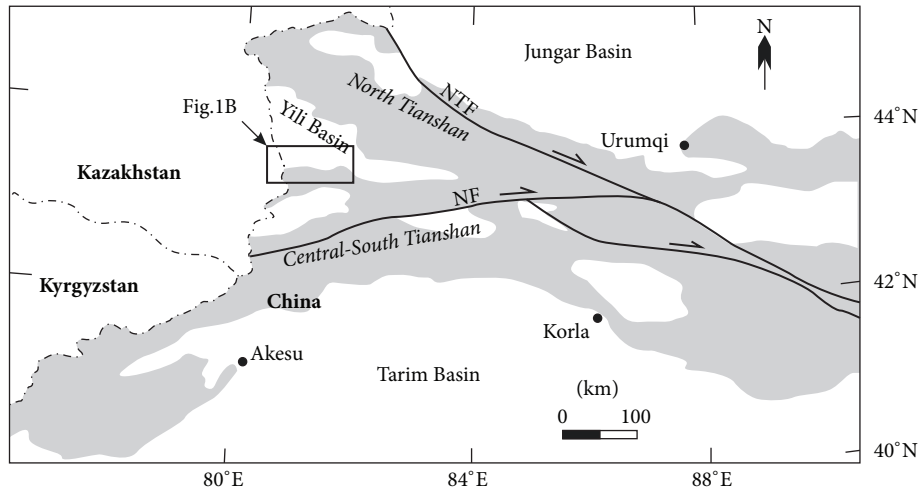
(a)
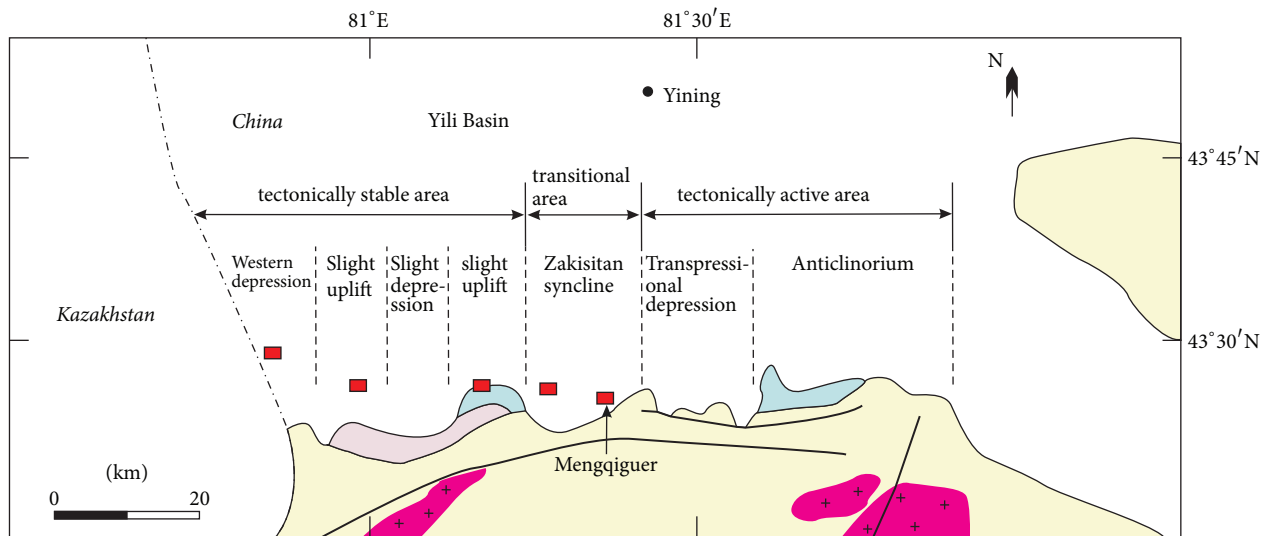
(b)

FIGURE 1: (a) Tectonic sketch map of the Yili Basin. (b) Sandstone-hosted uranium deposit distribution, lithologic units, and tectonic divisions in southern margin of the Yili Basin. All deposits are located in the transitional and tectonically stable areas, which consist of slight uplifts and depressions; in comparison, the tectonically active area contains no deposits. NTF: North Tianshan Fault; NF: Nalati Fault.

predominantly at, or near, the point of contact with underlying or overlying mudstone. The lengths of these orebodies range from 200 m to 600 m with thicknesses ranging from 0.2 m to 1.5 m. Lenticular orebodies typically occur close to the oxidation front, extend 100–300 m along the redox

front, and have thicknesses between 1.5 m and 3.2 m (occasionally 8.2 m depending on the scale of the host sandbody and oxidized lenticle). Roll-shaped ore bodies are the most commonly occurring shape; they are generally found in front of the interlayer oxidation zone, extend as far as 100–300 m,
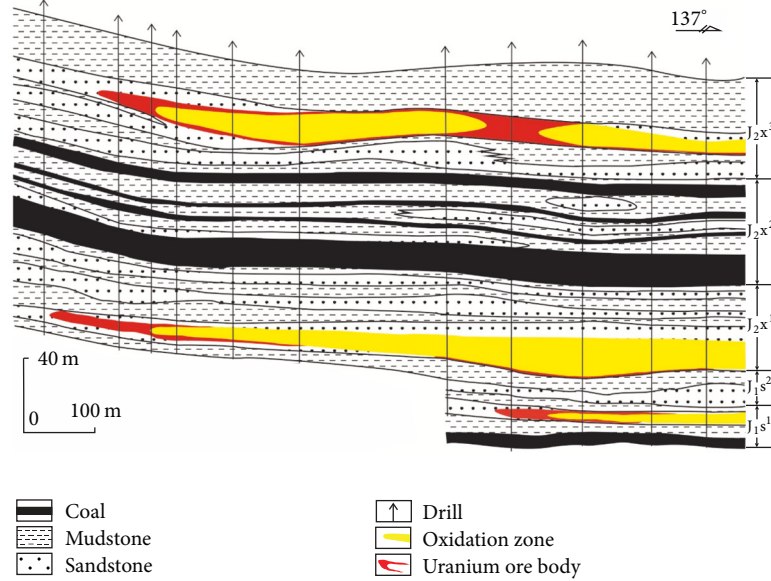
FIGURE 2: Host strata deposited several coal–sand–coal stacks represent braided river delta sediments. Orebodies occur at downsizing sites of host sandbodies and near contact zones with underlying or overlying mudstone. Lenticular orebodies are located in sandbodies of J_2x^3; roll-shaped and tabular orebodies are comparably located in sandbodies of J_1s^1 and J_2x^1.

TABLE 1: Altered minerals and geochemical indexes of each geochemical zone in the Mengqiguer uranium deposit.

Altered minerals and geochemical indexes	Oxidation zone		Transition zone (mineralized zone)	Primary zone
	Strong oxidation zone	Weak oxidation zone		
Colors	Red, light-red	Yellow, yellowish-white	Gray, grayish-white	Gray, dark-gray
Fe-minerals	Hematite, limonite	Limonite, rare pyrite	Pyrite, goethite	Pyrite, magnetite and siderite
Alterations	Hematitization, limonitization, kaolinization		Kaolinization, silicification, and uranium mineralization	Carbonation and chlorite
U-content (ppm)	4.0–6.0	6.5–20.6	>100	6.0–10.0
Total organic carbon (TOC) (wt%)	0.05–0.07	0.08–0.10	>0.5	>0.20
Fe^{3+}/Fe^{2+}	>0.9	0.5–0.8	0.3–0.5	0.2–0.4

have thicknesses between 1.5 m and 8.6 m, and are located in the downsizing sites of host sandbodies. However, orebody shapes do not present in isolation; a cross section shows that each shape is reworked into another.

An analysis of host rock colors, Fe-minerals, alteration, total organic carbon (TOC), and Fe^{3+}/Fe^{2+} shows that the interlayer oxidation zone of the Mengqiguer uranium deposit can be divided into an oxidation zone, transition zone (mineralized zone), and a primary zone. The oxidation zone can be further subdivided into a strong oxidation and weak oxidation zone (Table 1), where each zone tends to transition into the other. The strong oxidation zone is characterized by the highest Fe^{3+}/Fe^{2+} value (>0.9), the lowest TOC (0.05–0.07%), and U content (4.0–6.0 ppm), has strong hematitization and limonitization, and is red, or light-red, in color (Figure 3(a)). The weak oxidation zone contains rare carbon debris (TOC of 0.08–0.10%), limonite,

and rare pyrite (Fe^{3+}/Fe^{2+} of 0.5–0.8) and presents as a pale-yellow or yellowish-white color (Figure 3(b)). The transition zone (mineralized zone) has the highest TOC (>0.50%) and U content (>100 ppm), with weak silicification and strong kaolinization. The primary zone contains abundant pyrite, magnetite, and siderite and has moderate Fe^{3+}/Fe^{2+} values (0.2–0.4) and TOC (>0.20%). Both the mineralized and primary zones are rich in carbon debris and pyrite, and their rock colors are gray or grayish-white (Figures 3(c) and 3(d)).

3. Samples and Methods

Different to the methods used in previous studies, this study uses a representative sample collection of drill cores obtained from the entire interlayer oxidation zone. Samples consist of conglomerate, sandy conglomerate, and coarse- and medium-grained sandstone; 4 samples are obtained
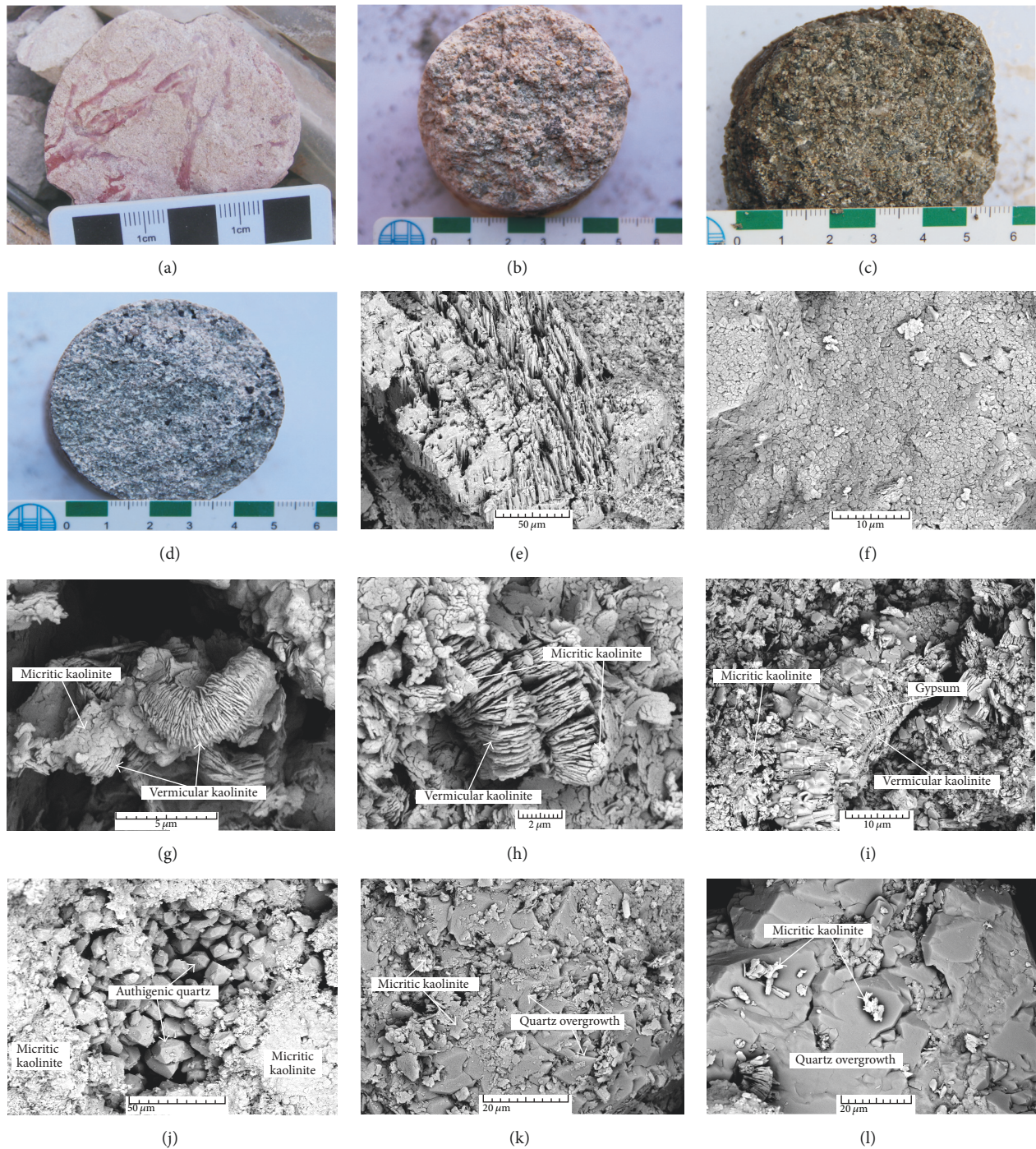
Figure 3: (a) Red sandstone with oxidized organic moulages in strong oxidation zone. (b) Yellowish-white sandy conglomerate dotted with red limonite in weak oxidation zone. (c) Gray mineralized sandy conglomerate. (d) Grayish-white sandstone containing carbon debris in primary zone. (e) Leached feldspar grain and pores filled with micritic kaolinite. (f) Micritic kaolinite covering quartz grains. (g) Vermicular kaolinite coexisting with micritic kaolinite. (h) Vermicular kaolinite superposed by micritic kaolinite. (i) Micritic kaolinite coexisting with gypsum and superposed upon vermicular kaolinite. (j) Authigenic quartz grains in intergranular pore covered by micritic kaolinite. (k) Strong quartz overgrowth covered by micritic kaolinite. (l) Quartz overgrowth replaced with micritic kaolinite.

from the strong oxidation zone, 14 samples from the weak oxidation zone, 4 samples from the mineralized zone, and 9 samples from the primary zone. In the mineralized zone, an HD-2000 handheld gamma radiometer (manufactured by the CNNC Beijing Research Institute of Uranium Geology) was used to screen samples from the drill cores. The measurement time used to screen each sample was 10 s, and ore samples with measured values of more than 100 Ur (ca. 100 ppm) were collected.

XRD analysis was conducted on all collected bulk core samples. In this respect, samples were firstly cleaned in an ultrasonic bath and then analyzed using a PANalytical X'Pert PRO X-ray diffractometer (Beijing Research Institute of Uranium Geology). The incident X-ray radiation was obtained using a line-focused PW3373/10 Cu X-ray tube operating at 40 kV and 40 mA, with an angle ranging from 5° to 90°. Mineral identification followed the procedures set out in Moore and Reynolds [37], and the Rietveld method of quantitative analysis was applied to obtain the relative abundance of the minerals.

In addition to XRD, an SEM-EDS (TESCAN-VEGAII LMU) (SEM) and LINK-ISISX alpha-ray spectrometer were used to differentiate the morphologies of kaolinite and investigate the association between kaolinite and uranium minerals. In this respect, samples were cut into $1 cm^3$ cubes and then gold-plated. Experiments were conducted at the Experimental Research Centre of the Research Institute of Petroleum Exploration & Development.

To determine the origin of kaolinite, a number of sandstones were obtained at various distances from the underlying coal seam. These sandstones were crushed and passed through a 80-mesh sieve; no less than 50 g of sample was then dissolved with hydrochloric acid in a beaker. Gas generated from the reaction between carbonate and hydrochloric acid was collected and passed through an alkaline solution to remove CO_2, prior to examination using a gas chromatograph (GC7890F) to determine the content of methane (C_1), ethane (C_2), propane (C_3), n-butane/isobutene (nC_4/iC_4), and n-pentane/isopentane (nC_5/iC_5), with an analytical precision of 0.05 μl/kg. In addition, Linkham THMSG-600 heating–freezing stage and Renishaw Invia Reflex-type confocal laser Raman microspectrometry were conducted at the Beijing Research Institute of Uranium Geology to analyze fluid inclusions in the secondary overgrowth zones, in microfractures of quartz grains, and in the carbonate. To test physicochemical properties of the fluids, temperature was tested using the homogenization method, and salinity was tested using the freezing method [38–41].

From the results of XRD analysis, samples with a high kaolinite content were selected for further tests. After cleaning, the selected bulk samples were crushed and passed through a 60-mesh sieve into a beaker filled with 500 ml distilled water, stirred for 3 min, and kept for 10 min. The suspension in the beaker was then moved to another beaker and dried to obtain the separation product (the main component was kaolinite). Based on XRD data, products with a kaolinite content of more than 80% were selected for H-O isotopic analysis, using the methods of Clayton and Mayeda [42] and

a Finnigan MAT253-type mass spectrometer. Oxygen gas was produced by treating the samples with BrF_5 in an externally heated nickel reaction vessel, and hydrogen was determined by treating H_2O with zinc at 550°C. SMOW was adopted as the standard, with a precision of ±2‰ for δD and ±0.2‰ for $\delta^{18}O$. All the above processes and analyses were conducted at the Key Laboratory of Uranium Resources Exploration and Evaluation Technology, CNNC.

4. Results

4.1. Content and Morphology of Kaolinite in Host Rocks. XRD results of host rocks from different geochemical zones are presented in Table 2. The average percentage clay mineral content in all geochemical zones varies between 10.9% and 17.5% (percentage contents of clay minerals in the strong and weak oxidation zones are 13.7% and 15.1%, resp.; 17.5% in the mineralized zone; and 10.9% in the primary zone). Kaolinite is the dominant clay mineral (accounting for 50.7–72.5% of clay minerals), followed by mixed illite/smectite and illite. The highest average content of kaolinite reaches 72.5% in the grayish-white host rocks within the mineralized zone; the content increases from the strong oxidation zone to the mineralized zone and decreases sharply in the primary zone.

Based on the SEM observations, kaolinite in the host rocks is found to be mainly vermicular and micritic. Micritic kaolinite is found in both intergranular pores and pores within dissolved feldspar grains (Figure 3(e)) or dispersed on the surface of quartz and other grains (Figure 3(f)). It has an irregular form, dissolved margins, and pseudohexagonal crystal plates, with crystal sizes varying between 2 μm and 5 μm. Vermicular kaolinite, in contrast, has large pseudo-hexagonal plate crystals with regular crystal edges and crystal sizes ranging between 10 μm and 20 μm.

Vermicular kaolinite is rare and is mostly found in the gray or grayish-white sandstones of the primary and mineralized zones and occasionally in the weakly oxidized sandstones. Micritic kaolinite is more common and is found in sandstones within the oxidation and mineralized zones. In the sandy conglomerates of the oxidation zone, which have good porosity, micritic kaolinite is dispersed on the surface of grains and is superposed upon vermicular kaolinite (Figures 3(g) and 3(h)). In addition, gypsum growing on the surface of vermicular kaolinite (Figure 3(i)) is possibly formed under the same conditions as micritic kaolinite. Authigenic quartz grains and quartz overgrowth are widespread in the host rocks, particularly in the mineralized zone. Generally, numerous authigenic quartz grains are formed in intergranular pores and covered by micritic kaolinite (Figure 3(j)). Strong quartz overgrowth occasionally blocks the pores of sandstones and is also covered and replaced with micritic kaolinite (Figures 3(k) and 3(l)). From these results, it is proposed that the authigenic quartz and quartz overgrowth possibly formed during diagenesis, earlier than the formation of micritic kaolinite.

Based on the replacing relationships described above, a paragenetic sequence associated with kaolinite in the Mengqiguer uranium deposit was constructed and is illustrated in Figure 4 (where dashed lines are used to represent

TABLE 2: Average percentage content of clay minerals in host rocks from each geochemical zone.

Geochemical zones	Sampling depth (m)	Number	Framework grains (%)						Clay minerals (%)		
			Qtz	Kfl	Pl	Cal	Dol	Clay	Kao	It	I/S
Oxidation zone											
Strong oxidation zone	364–425.8	4	68.4	5.9	6.6	2.2	1.2	13.7	62.5	11.5	26
Weak oxidation zone	320–623	14	67.4	7.5	6.3	1.9	1.8	15.1	69.8	11	19.2
Mineralized zone	456.5–604.9	4	66.2	6.2	5.2	3.3	1.6	17.5	72.5	10.2	17.3
Primary zone	367–650.5	9	67.5	5.9	8	5	2.7	10.9	50.7	19.3	30

Qtz, quartz; Kfl, potash feldspar; Pl, plagioclase; Cal, calcite; Dol, dolomite; Kao, kaolinite; It, Illite; I/S, illite/smectite mixed-layer.

Minerals	Early ⟶ Late		
	Primary zone	Oxidized zone	Mineralized zone
Authigenic quartz	—————	——————	—————
Quartz overgrowth	—————	- - - - - - - -	—————
Feldspar-leaching		—————	- - - - - - - -
Vermicular kaolinite	—————	- - - - - - - -	—————
Micritic kaolinite		—————	—————
Gypsum		—————	—————

FIGURE 4: Paragenetic sequence of the Mengqiguer uranium deposit.

minerals at a relatively weak intensity, or decreasing amounts of minerals, as determined using microscopic observations). Authigenic quartz grains, quartz overgrowth, and vermicular kaolinite are observed in all geochemical zones and belong to the diagenetic stage. Feldspar-leaching, micritic kaolinite, gypsum that pervasively cover or replace quartz overgrowth, and vermicular kaolinite observed in the oxidized and mineralized zones are assigned to the mineralization stage. Quartz overgrowth and vermicular kaolinization are noted to be relatively weak in the oxidized and mineralized zones, and this is partly because they are replaced with micritic kaolinite.

4.2. Association between Kaolinization and Uranium. SEM observations combined with measurement results of EDS indicate that uranium minerals and micritic kaolinite fill in the dissolved pores of K-feldspar and intergranular pores (Figures 5(a) and 5(b)). Uranium minerals (uraninite) generally occur as grape-like crystals imbedded in micritic kaolinite (Figures 5(c) and 5(d)). In addition, uranium is adsorbed by micritic kaolinite, forming a kaolinite–uranium complex with an amorphous state (Figures 5(e), 5(f), 5(g), and 5(h)). Micritic kaolinite has a close association with uranium mineralization.

4.3. Gas Hydrocarbon in Host Rocks. Results of gas hydrocarbon analysis of host rocks are shown in Table 3. Of these gases, the methane (C_1) content is dominant (but it decreases sharply with an increase in distance from the underlying coal seam), followed by ethane (C_2) and then propane (C_3). Other gases (such as nC_4, iC_4, nC_5, and iC_5) are present in minor amounts. Consequently, the C_1/C_2^+ and $C_1/\sum C$ values are elevated and range from 11.71 to 21.98 and 0.92 to 0.96, respectively; there is an irregular increase in these values with respect to the increase in distance from the underlying coal seam.

4.4. Fluid Inclusions

4.4.1. Fluid Inclusion Petrography. Based on the components of inclusions and the phase assemblages present at room temperature, five types of fluid inclusions were identified: (1) aqueous inclusions (liquid + vapor) (AI) with a vapor percentage of <50%, (2) liquid hydrocarbon monophase inclusions (LH), (3) hydrocarbon-aqueous biphase inclusions (liquid + liquid) (HA), (4) gas monophase inclusions (GI), and (5) gas-aqueous inclusions (GA) with a vapor percentage of <50%.

Although relatively rare, LH and HA inclusions are generally present together, have elliptical and subrounded shapes, and coexist with AI inclusions (Figure 6(a)), thereby suggesting low temperatures and immiscibility trapping features. They present with a blue fluorescence color (Figure 6(b)) and occur primarily along healed microfractures that terminate at the overgrowth boundary in quartz grains and in carbonate cement (Figure 6(c)). There were no LH and HA inclusions

(a)

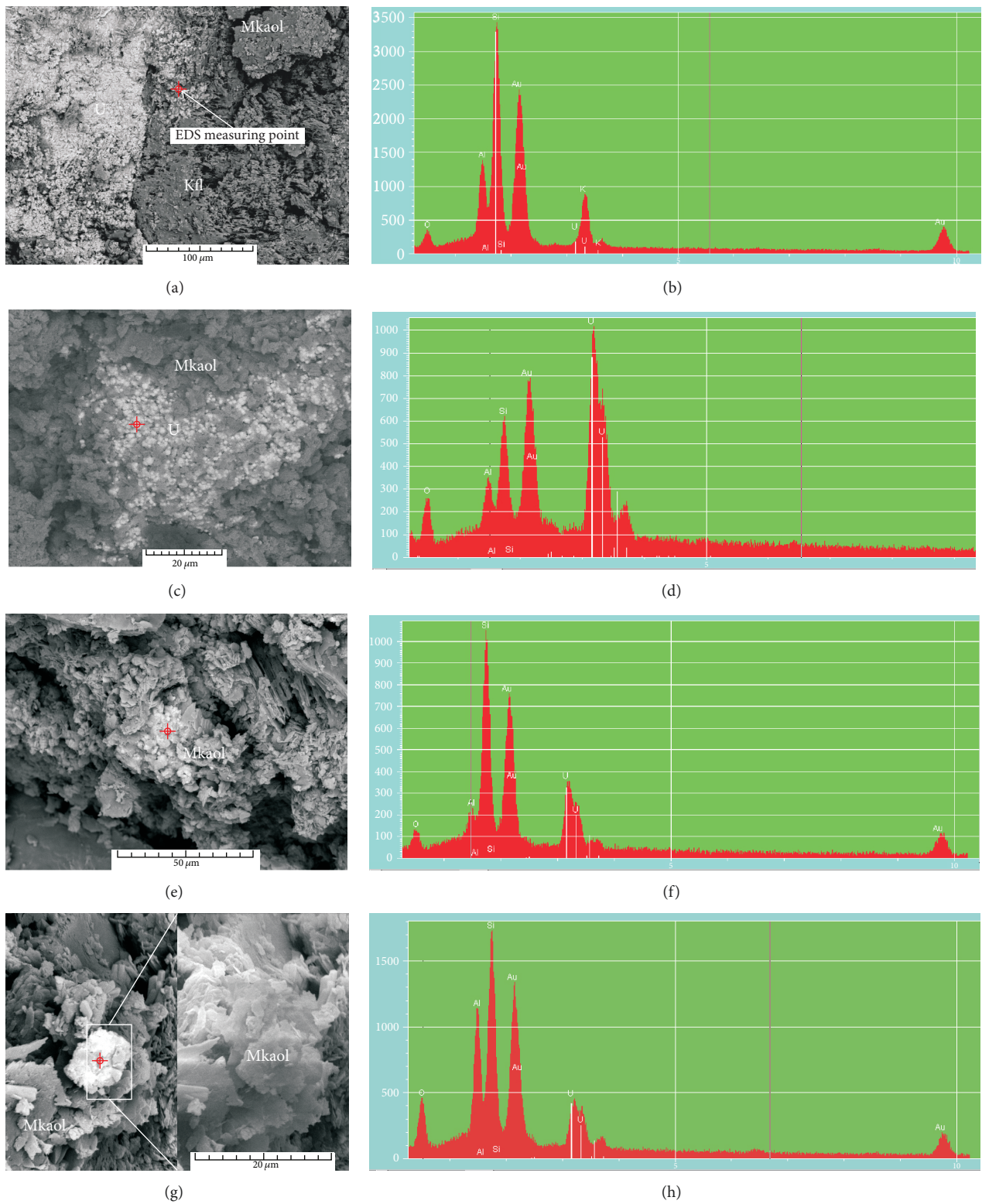(b)

(c)

(d)

(e)

(f)

(g)

(h)

Figure 5: (a) Uranium minerals and micritic kaolinite filling-in leached pores of K-feldspar. (b) EDX analysis of area in (a). (c) Grape-like uraninite imbedded in stacks of micritic kaolinite. (d) EDX analysis of area in (c). (e) Micritic kaolinite adsorbing uranium (white area). (f) EDX analysis of area in (e). (g) Micritic kaolinite stack adsorbing uranium (white area). (h) EDX analysis of area in (g). Mkaol: micritic kaolinite; U: uranium mineral; Kfl: K-feldspar.

TABLE 3: Gas hydrocarbon composition in host rocks within the Mengqiguer uranium deposit.

Samples	Distance from underlying coal seam (m)	Rocks	C_1 (μl/kg)	C_2 (μl/kg)	C_3 (μl/kg)	nC_4 (μl/kg)	iC_4 (μl/kg)	nC_5 (μl/kg)	iC_5 (μl/kg)	C_1/C_2^+	$C_1/\sum C$
P-1	12	Coarse-grained sandstone	910.20	35.34	10.72	0.78	3.63	0.37	1.00	17.56	0.95
P-2	13	Coarse-grained sandstone	908.40	30.34	15.56	0.83	1.05	0.23	0.76	18.63	0.95
P-3	21	Conglomerate	675.21	18.61	10.01	0.33	1.56	0.17	0.44	21.70	0.96
P-4	29	Medium-grained sandstone	364.33	12.81	5.52	0.46	2.11	0.29	0.65	16.68	0.94
P-5	35	Sandy conglomerate	200.30	9.81	4.70	0.39	1.56	0.19	0.45	11.71	0.92
P-6	44	Fine-grained sandstone	194.32	6.82	4.10	0.37	1.41	0.20	0.44	14.57	0.94
P-7	49	Medium-grained sandstone	88.80	2.51	1.01	0.09	0.34	<0.05	0.09	21.98	0.96

C_1, methane; C_2, ethane; C_3, propane; nC_4, n-butane; iC_4, isobutene; nC_5, n-pentane; iC_5, isopentane; $C_2^+ = C_2 + C_3 + nC_4 + iC_4 + nC_5 + iC_5$; $\sum C = C_1 + C_2 + C_3 + nC_4 + iC_4 + nC_5 + iC_5$.

found in quartz overgrowth zones or at the quartz overgrowth boundary.

GI inclusions with a subrounded shape are relatively abundant in samples (Figure 6(d)), and present with a yellow-white fluorescence color (Figure 6(e)). Raman spectroscopic analysis confirms the presence of methane inclusions (Figure 6(f)). GI inclusions rarely occur alone and frequently coexist with GA inclusions; both occur primarily along healed microfractures in quartz grains and carbonate cement, some of which contain coexisting AI inclusions with dimensions of 2–15 μm.

AI inclusions are abundant in all samples; they are typical two phase inclusions, present with rounded and subrounded shapes, and have small vapor bubbles at room temperature. Their sizes vary greatly and are generally between 2 μm and 18 μm in diameter, with minimum and maximum dimensions of 2 μm × 2 μm and 15 μm × 20 μm, respectively. Most AI inclusions occur along healed microfractures (Figure 6(g)) and unhealed microfractures in quartz grains (which do not terminate at the contact between detrital grains) and quartz overgrowth (Figure 6(h)). A small percentage of aqueous inclusions occur in quartz overgrowth zones (Figure 6(i)). AI inclusions coexisting with other types of inclusions occur much less frequently.

4.4.2. Microthermometry. AI inclusions hosted in quartz healed and unhealed microfractures, and in overgrowth zones (particularly those coeval with LH or GI inclusions in a microfracture), were selected for microthermometric analysis, and the fluid inclusion assemblage (FIA) concept [43] was used to guide microthermometric analysis. Randomly distributed fluid inclusions in carbonate cement were not

adopted for microthermometric analysis, because it is difficult to identify that they were entrapped at the same time (i.e., belonging to an FIA) [44]. Homogenization temperatures (T_h) and ice-melting temperatures ($T_{m\text{-ice}}$) were determined for AI inclusions with relatively low vapor percentages (<15%) and capability of homogenizing to a single liquid phase.

Microthermometric and salinity data of AI inclusions in ore-bearing sandstones are listed in Table 4. AI inclusions in quartz healed microfractures have T_h values ranging from 64°C to 76°C and salinities from 0.4 wt% NaCl$_{eq}$ to 6.6 wt% NaCl$_{eq}$. The T_h values of AI inclusions coeval with GI and LH in quartz healed microfractures have similar distribution ranging from 71°C to 78°C and 69°C to 74°C, respectively, with salinities from 8.4 wt% NaCl$_{eq}$ to 11.0 wt% NaCl$_{eq}$, and 7.6 wt% NaCl$_{eq}$ to 8.3 wt% NaCl$_{eq}$, respectively. AI inclusions in quartz overgrowth zones have T_h values ranging between 75°C and 86°C and salinities from 3.4 wt% NaCl$_{eq}$ to 7.4 wt% NaCl$_{eq}$. The T_h value range of AI inclusions in quartz unhealed microfractures varies between 51°C and 63°C, with salinities from 1.2 wt% NaCl$_{eq}$ to 3.7 wt% NaCl$_{eq}$.

Generally, the T_h values of AI and AI coeval with GI and LH inclusions in the quartz healed microfractures have a wide range, mainly varying between 65°C and 75°C (Figure 7). In particular, there are relatively higher T_h values for AI coeval with GI and LH inclusions (70–75°C). AI inclusions in the quartz overgrowth zones have the highest T_h values, and those in the quartz unhealed microfractures have the lowest T_h values. Salinity values increase slightly with T_h values: the lowest values are found in AI inclusions of unhealed microfractures, and the highest values are found in AI coeval with GI inclusions of healed microfractures.
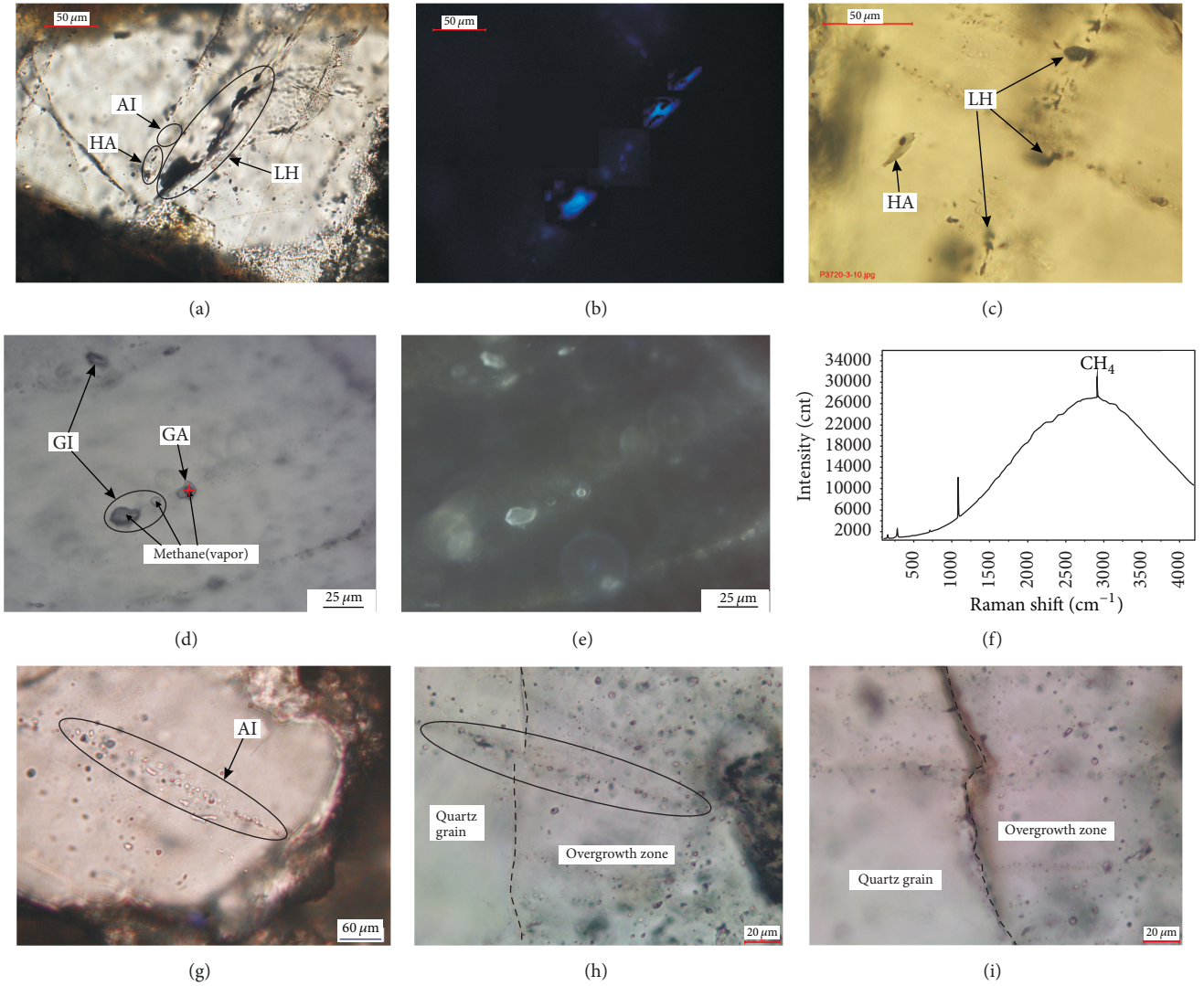
FIGURE 6: (a) LH inclusions coexisting with HA and AI inclusions occurring along healed microfractures in quartz grain. (b) Blue fluorescence color of LH and HA inclusions shown in Figure 6(a). (c) LH and HA inclusions with elliptical shapes in carbonate cement. (d) Coexistence of GI and GA inclusions in carbonate cement. (e) Yellowish-white fluorescence color of GI and GA inclusions in carbonate cement. (f) Vapor composition of GA inclusion analyzed by Raman spectrum (red cross in Figure 6(d) represents measurement point). (g) Linear group of AI inclusions occurring along healed microfracture in quartz grain. (h) Linear group of AI inclusions occurring along unhealed microfracture cross-cutting quartz overgrowth zone. (i) Random distribution of AI inclusions in quartz overgrowth zone.

TABLE 4: Microthermometric and salinity data of fluid inclusions in ore-bearing rocks within the Mengqiguer uranium deposit.

Mineral	Host site	Type	Number	Size (μm)	$T_{m\text{-ice}}$ (°C)	T_h (°C)	Salinity $w(\text{NaCl}_{eq})\%$
		AI	43	2 to 18	−6.5 to −2.1	64–76	3.5–9.7
	Healed micro-fractures	AI coeval with GI	16	2 to 10	−7.4 to −5.4	71–78	8.4–11.0
Quartz		AI coeval with LH	9	2 to 12	−5.3 to −4.8	69–74	7.6–8.3
	Overgrowth zones	AI	21	2 to 14	−4.7 to −2.0	75–86	3.4–7.4
	Unhealed micro-fractures	AI	26	2 to 8	−1.3 to −0.7	51–63	1.2–3.7

4.4.3. Aqueous Inclusion Trapping Pressure. The coexistence of AI and LH/GI inclusions within an individual FIA is interpreted to indicate fluid immiscibility [45]. Although vapor-only inclusions may be produced by necking-down or postentrapment stretching [43, 46], their widespread occurrence and abundance in the examined samples contradicts such interpretations. Thus, AI inclusions with the lowest vapor percentages are considered to represent an homogeneously entrapped liquid phase, and the GI inclusions represent an homogeneously entrapped vapor phase. Furthermore, the T_h
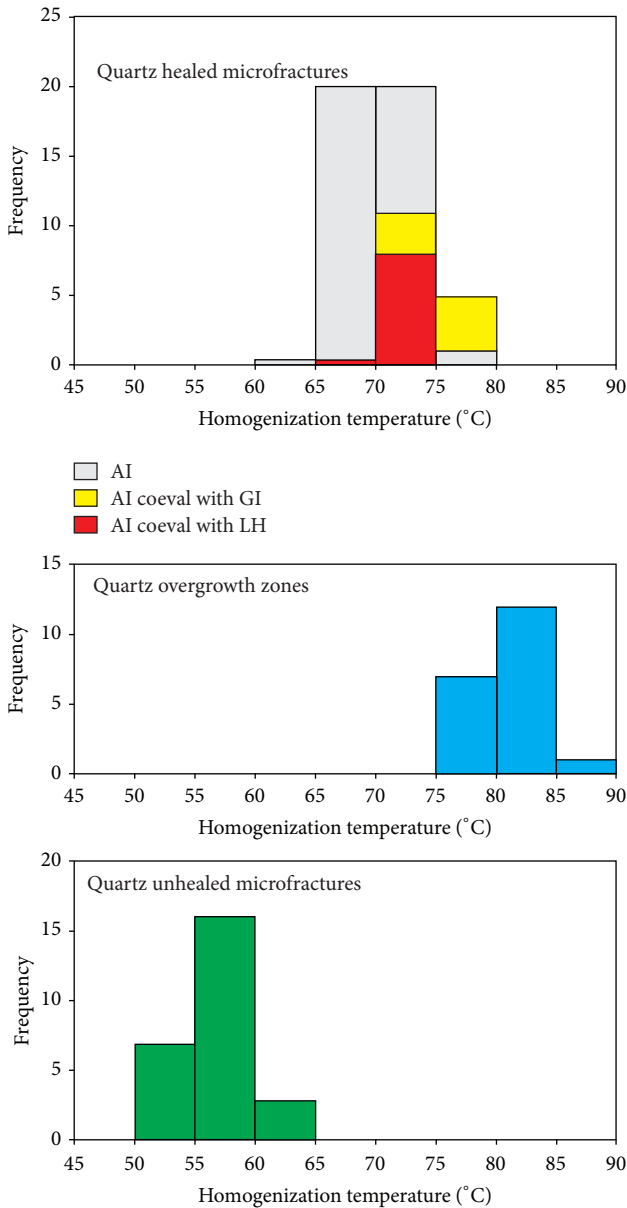
FIGURE 7: Histogram for homogenization temperatures of fluid inclusions in quartz healed microfractures, overgrowth zones, and unhealed microfractures.

□ Strong oxidation zone
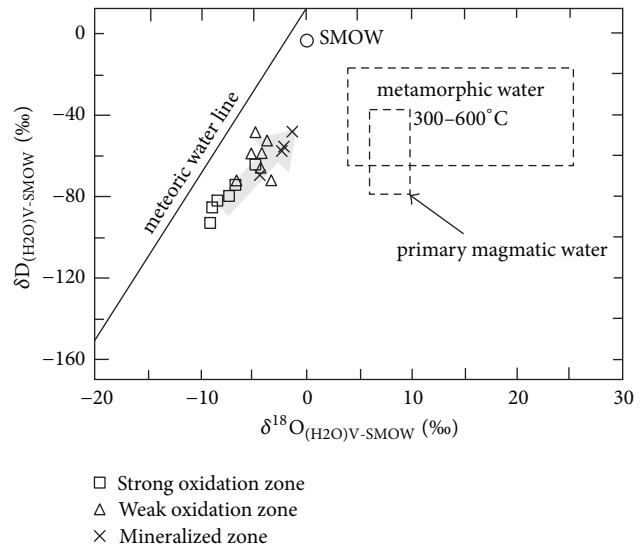△ Weak oxidation zone
× Mineralized zone

FIGURE 8: Plot of δD versus $\delta^{18}O$ for kaolinite-forming fluid in the Mengqiguer uranium deposit. Fields for SMOW, metamorphic water, primary magmatic water, and meteoric water lines are referred to Taylor Jr. [32].

values of AI inclusions with the lowest vapor percentages represent trapping temperatures, and no pressure correction is required. Accordingly, fluid pressures (P_h) at homogenization temperatures represent trapping pressures [45]: P_h values of AI coeval with GI and LH inclusions in the quartz healed microfractures calculated with FLUIDS (Bakker 2003) cover a range from 5 bar to 6 bar.

4.5. O and H Isotopic Compositions of Kaolinite. The O and H isotopic compositions of kaolinite-dominated clay minerals with a kaolinite purity of >80% are listed in Table 5. With respect to the low temperature of kaolinite formation in this study, $\delta^{18}O_{(H2O)V\text{-}SMOW}$ values were calculated based on the fractionation equation between minerals and water following Savin [47]. As micritic kaolinite is dominant in the extracted kaolinite-dominated clay minerals, it is considered that the O and H isotope data in Table 5 are related to fluid associated with micritic kaolinite formation. As micritic kaolinite was formed after quartz overgrowth, with respect to the result of the paragenetic sequence analysis presented in Figure 4, the maximum T_h values of AI inclusions in the quartz unhealed microfractures were used to calculate $\delta^{18}O_{(H2O)V\text{-}SMOW}$ values: these range from −9.1‰ to −4.8‰ in the strong oxidation zone, from −6.6‰ to −3.3‰ in the weak oxidation zone, and from −4.4‰ to −1.3‰ in the mineralized zone, with a gradually elevating trend. The same trend can be seen in the $\delta D_{(H2O)V\text{-}SMOW}$ values between the strong oxidation zone and the mineralized zone, where the kaolinite-forming fluid underwent sufficient water-rock reaction and O and H isotopic fractionation. Figure 8 shows that all of the $\delta D_{(H2O)V\text{-}SMOW}$ and $\delta^{18}O_{(H2O)V\text{-}SMOW}$ values fall closely under the meteoric water line, which indicates that either no metamorphic water was involved in kaolinite formation, or primary magmatic water was involved. These results could also indicate that surface meteoric fluid was responsible for the formation of micritic kaolinite, and, in combination with the analysis of kaolinite morphology presented in this study, it is suggested that the micritic kaolinite is closely associated with uranium mineralization.

5. Discussion

5.1. Origin of Ore-Forming Fluids. The vermicular and micritic kaolinite and the five types of fluid inclusions suggest that the host rocks underwent two types (or stages) of fluid alteration. The LH, HA, and GA inclusions present with blue and yellowish-white fluorescence, which indicates the

TABLE 5: O and H isotopic compositions of extracted kaolinite from altered zones in the Mengqiguer uranium deposit.

| Altered zones | Sample | Mineral | Clay minerals (%) | | | | | O and H isotopic compositions (‰) | | |
			S	C	I/S	It	Kao	$\delta D_{(H2O)V\text{-}SMOW}$	$\delta^{18}O_{V\text{-}SMOW}$	$\delta^{18}O_{(H2O)V\text{-}SMOW}$
Strong oxidation zone	K1	Extracted kaolinite	/	/	/	13	87	−82.1	8.6	−8.4
	K2	Extracted kaolinite	2	/	/	14	84	−83.4	8.1	−8.9
	K3	Extracted kaolinite	/	/	/	11	89	−80.4	9.7	−7.3
	K4	Extracted kaolinite	/	/	/	18	82	−64.4	12.2	−4.8
	K5	Extracted kaolinite	3	/	/	12	85	−92.8	7.9	−9.1
	K6	Extracted kaolinite	/	/	/	10	90	−81.1	9.3	−7.7
Weak oxidation zone	K7	Extracted kaolinite	/	/	/	13	87	−58.8	11.8	−5.2
	K8	Extracted kaolinite	/	/	/	17	83	−49.2	12.2	−4.8
	K9	Extracted kaolinite	/	/	/	10	90	−71.9	10.4	−6.6
	K10	Extracted kaolinite	/	/	/	17	83	−59.3	12.8	−4.2
	K11	Extracted kaolinite	/	/	7	9	84	−72.0	13.7	−3.3
	K12	Extracted kaolinite	/	/	/	17	83	−53.2	13.3	−3.7
	K13	Extracted kaolinite	/	/	/	14	86	−61.1	12.4	−4.6
Mineralized zone	K14	Extracted kaolinite	/	/	/	11	89	−70.1	12.6	−5.2
	K15	Extracted kaolinite	10	/	/	8	82	−48.4	12.7	−5.1
	K16	Extracted kaolinite	10	/	/	7	83	−56.4	12.9	−4.9
	K17	Extracted kaolinite	5	/	/	9	86	−58.2	14.2	−2.6

/, below detecting limit; Kao, kaolinite; It, illite; I/S, illite/smectite mixed-layer. C, chlorite; S, smectite.

presence of a hydrocarbon-bearing fluid. In addition, the volatile components in the GA inclusions identified by laser Raman suggest that the hydrocarbon-bearing fluid contains CH_4. Results of gas hydrocarbon analysis of host rocks show that the contents of CH_4 in samples from overlying sandstones adjacent to the coal seam are relatively higher than those in other samples. Additionally, the elevated values of C_1/C_2^+ and $C_1/\sum C$ vary (11.71–21.98 and 0.92–0.96, resp.) and fall in a range representing a coal-derived origin [48]. Based on carbon isotope analysis in the southern margin of the Yili Basin and with respect to the decarboxylation of OM that produces organic acids, Wu et al. [49] determined that hydrocarbons in the ore-forming fluid originate from coal beds within the strata. It thus can be concluded that the hydrocarbon-bearing fluid containing CH_4 in the host rocks is an organic acidic fluid that was generated from OM during diagenesis.

In addition, the O and H isotope compositions of micritic kaolinite present a regular increase from the strong oxidation zone to the mineralized zone, which is indicative of the formation of micritic kaolinization and oxidation zones via meteoric water infiltration. It is interpreted from these results, and the close relationship between micritic kaolinite and uranium minerals evidenced by SEM observation that oxygen-rich interlayer infiltration fluid (characterized by meteoric water) was involved in uranium mineralization. It is also inferred that the interlayer oxidation fluid played a crucial role in ore formation, owing to the spatially close association between ore bodies and oxidation zones.

Fluid immiscibility, inferred from the coexistence of liquid-dominated and vapor-dominated fluid inclusions within individual FIA in quartz healed microfractures, indicates a shallow-burial environment [45]. Hydrocarbon-bearing fluid inclusions confined in the quartz healed microfractures that terminate at the overgrowth boundary suggest that the hydrocarbon-bearing fluid was produced during the shallow-burial diagenetic stage, which is characterized by low T_h values ranging from 69°C to 78°C, relatively high salinity values (7.6–11.0 wt% $NaCl_{eq}$), and low trapped pressures (5-6 bar). Fluid inclusions in the quartz overgrowth zones are interpreted as primary inclusions occurring during diagenesis [50]. The AI-only inclusions in the quartz overgrowth zones suggest that no hydrocarbon was present in the pore fluid during this diagenesis or that a rare hydrocarbon existed. Fluid inclusions in the quartz unhealed microfractures record postdiagenesis pore water migration [50], and AI inclusions in the quartz unhealed microfractures are characterized by low T_h values (51–63°C) and low salinity values (1.2–3.7 wt% $NaCl_{eq}$), which represent a supergene meteoric water origin that can be interpreted as an ore-forming fluid. This result is also supported by the H-O isotopic plot (Figure 8).

5.2. Kaolinite Genesis. The varying clay mineral content suggests that intensive argillization occurred within the oxidation and mineralized zones. The regular changes in the kaolinite content observed in drill cores from oxidation zone to mineralized zone suggest that intense kaolinization in the mineralized zone was mostly formed in the oxidation zone but migrated to the mineralized zone via pore fluid. Based on SEM observations, vermicular kaolinite is mainly found in intergranular pores in sandstones and is widely interpreted to have been formed during shallow burial (<2000 m) in a stable diagenetic environment [51, 52]. The later-formed micritic kaolinite is superposed upon vermicular kaolinite and may be related to rapid crystallization under supergene conditions.
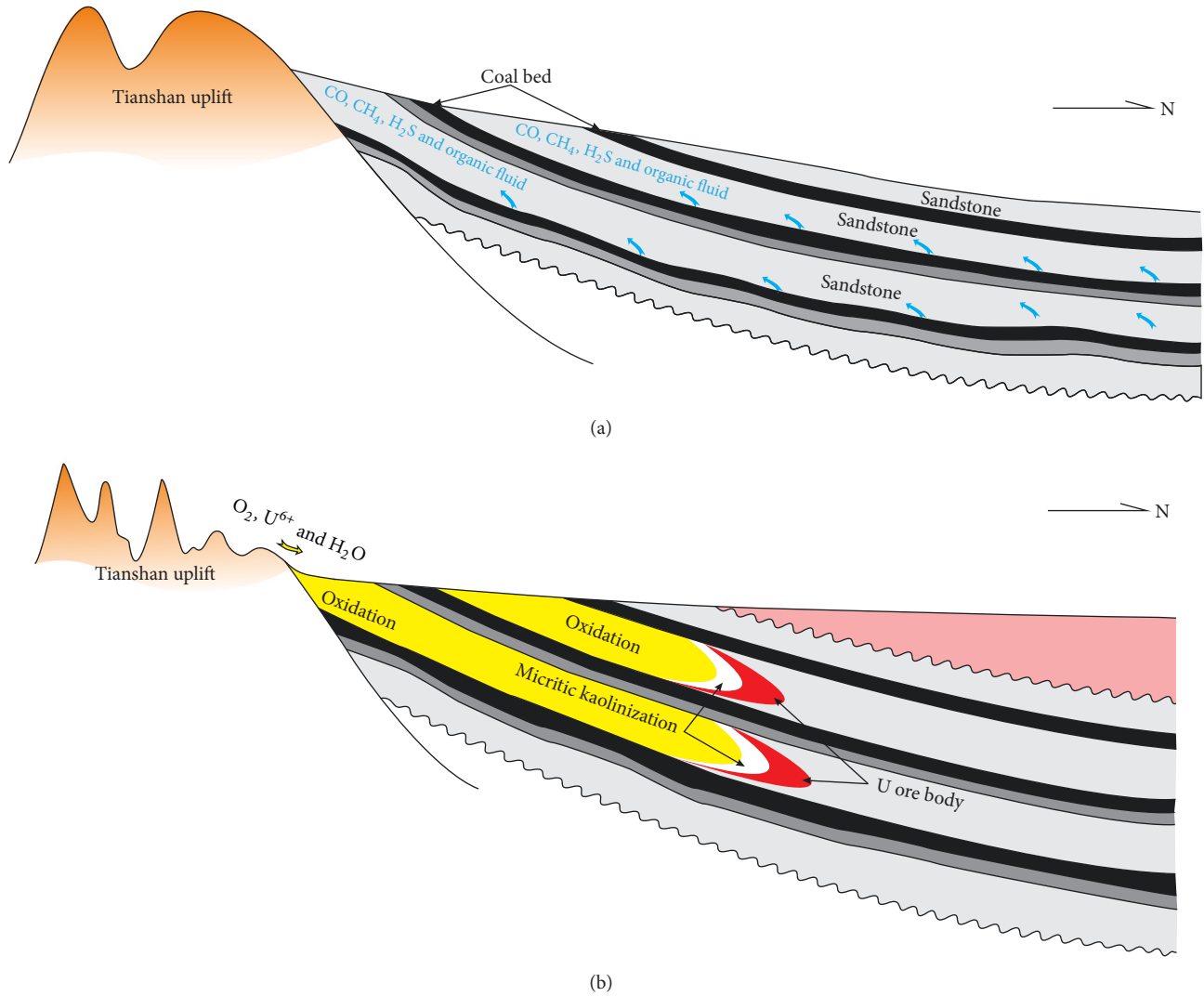
(a)

(b)

FIGURE 9: (a) Organic fluid containing CO, CH_4, and H_2S occurred from coal beds and carbonaceous mudstones during shallow-burial diagenetic stage and entered into sandstones while flowing from the basin bottom to top. (b) Meteoric water containing U and O_2 infiltrated interlayered sandstones, forming oxidation zones, white micritic kaolinization zones, and uranium orebodies.

In addition, the H-O isotopic plot suggests that surface meteoric fluid is responsible for the micritic kaolinite and uranium mineralization. Furthermore, as micritic kaolinite is closely associated with uranium mineralization and is formed by ore-forming fluids, the results of micritic kaolinite O and H isotopes constrain the origin and evolution of the ore-forming fluids.

The thermal evolution of OM (coal and carbon debris) in the target strata increased with its burial depth during burial diagenesis. Vitrinite reflectance (Ro) of the coal beds in the mining area is 0.40–0.74% [36], suggesting that OM is semi-mature to weakly mature, which corresponds to the late-early diagenesis or early-middle diagenesis [53]. Generally, when Ro = 0.35%, decarboxylation of OM forms organic acids and enriches hydrothermal fluid with CO, H_2S, and CH_4 [54, 55]. There is an increase in the amount of organic acids with an increase in burial depth and geothermal gradient [56]. During sedimentation and subsidence of the basin, compaction occurred and fluids flowed from the low-permeability coals, shales, and carbonaceous mudstones to the adjacent high-permeability sandstones, in a direction from bottom to top and from center to edge (Figure 9(a), Cartwright [57]; Xue et al. [58]). When a rich organic acid flow entered sand-stones, aluminosilicate and carbonate minerals were dissolved and secondary pores were formed. Simultaneously, authigenic minerals, such as vermicular kaolinite and quartz overgrowths, also formed. The clay mineral content in the mining area and scanning electron microscopy data evidence an obvious and widespread alteration of sandstones by acidic fluid, and the replacement of vermicular kaolinite with micritic kaolinite.

The basin has undergone uplifting and shrinkage since the Miocene [59, 60] and basin fluids have changed in action from seeping to permeating. Terrain elevation differences and pressures owing to tectonic compression are the major fluid-driving forces. The basin fluids generally flowed from

top to bottom and from edge to center [61]. Meteoric water contained O_2 and CO_2, was strongly oxidizing and weakly acidic, and it leached the feldspars within the sandstones, thereby forming the micritic kaolinite that filled leached pores and superimposed upon the previously formed vermicular kaolinite and other grains. The feldspar grains that were replaced with micritic kaolinite are more frequently identified in the red or yellow shallow sandstones than those in the deep-gray sandstones. Superimposed micritic kaolinite is observed in all sandstone samples collected from the oxidation and mineralized zones, which suggests that ore-bearing sandstones underwent intense leaching by oxidizing meteoric water.

5.3. Uranium Mineralization. Braided river delta sediments with coal–sand–coal stacks were deposited in the target strata (J_1s and J_2x). This rock assemblage offered conducive infiltration for phreatic water in the permeable layer (sandstone) between impermeable layers (coal and mudstone), and an interlayer oxidation zone was thus developed.

During diagenesis, secondary pores formed in the sandstones that was altered by early organic acidic fluid, which then increased permeability and created pore-space for the later long-term infiltration of meteoric water containing U and O_2. The gas-charging effects of CO, H_2S, and CH_4 greatly enhanced the reduction capacity of the host sandstones, which favored subsequent uranium reduction and enrichment. In addition, the humic acid and fulvic acid in the organic acidic fluid leached uranium from the surrounding rocks to form uranyl-organic complexes and preconcentrated the uranium [21, 62–66].

Since the Miocene, meteoric water containing U and O_2 infiltrated interlayered sandstones that were rich in pyrite and carbon debris. The abundant pyrite and carbon debris, both of which are highly effective reducers for uranium, favored the rapid reduction of U^{6+} in oxidized water to U^{4+} which precipitated as solid uraniferous mineral from the solution. Therefore, the sandbodies between two coal seams were ideal for forming an interlayer oxidation zone and uranium mineralization. As the oxidation of pyrite and carbon debris caused by meteoric water, sulfuric and organic acids were generated and lowed the pH of the interlayer fluid and then transformed the alkalescent interlayer fluid to neutral or weakly acidic in the redox front. This process produced micritic kaolinite that sorbed $(UO_2)^{2+}$ (uranyl) through cation exchange, forming uranium-kaolinite complexes, and also reduced U^{6+} in the interlayer fluid to U^{4+} by the pyrite and carbon debris at the acid oxidation front (Figure 9(b)).

6. Conclusions

Intense kaolinization is common in ore-hosting rocks and is related to the leaching of feldspar by acidic fluid. The well-formed vermicular kaolinite is attributed to hydrocarbon-bearing fluid formed during shallow diagenesis, with low T_h values and high salinity values. In contrast, irregular micritic kaolinite is attributed to meteoric fluid, with low T_h values and low salinity values.

During the shallow-burial diagenetic stage of the target strata, thermal evolution of OM in the coal-bearing clastic rocks produced hydrocarbon-bearing fluid, which moved to the adjacent sandstones and enhanced their reduction capacity. Silicate minerals, such as feldspar, were leached and formed vermicular kaolinite with secondary pores, offering a favorable space for uranium mineralization. As the meteoric fluid containing U and O_2 infiltrated the interlayer sandstones, oxidation zone occurred and formed a micritic kaolinite adsorbed uranyl forming U-bearing kaolinite complex. Furthermore, uranium precipitation and enrichment occurred at the acidic oxidation front.

The results of this study confirm that intense kaolinization in sandstones of coal-bearing clastic rocks is closely associated with uranium mineralization. Therefore, to a certain extent, micritic kaolinization can be used as an effective indicator for prospecting sandstone-hosted uranium deposits in coal-bearing clastic rocks.

Conflicts of Interest

The authors declare that there are no conflicts of interest regarding the publication of this paper.
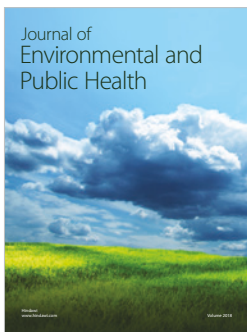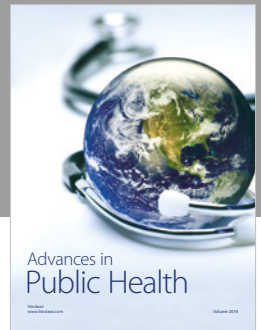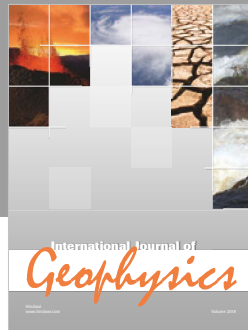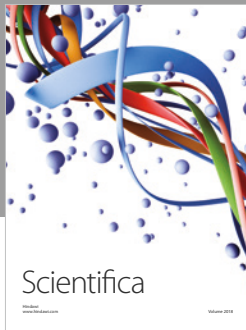
Acknowledgments

References

[1] J. C. Baker and S. D. Golding, "Occurrence and palaeohydrological significance of authigenic kaolinite in the aldebaran sandstone, denison trough, Queensland, Australia," *Clays and Clay Minerals*, vol. 40, no. 3, pp. 273–279, 1992.

[2] G. Chen, G. Du, G. Zhang, Q. Wang, C. Lv, and J. Chen, "Chlorite cement and its effect on the reservoir quality of sandstones from the Panyu low-uplift, Pearl River Mouth Basin," *Natural Gas Geoscience*, vol. 8, no. 2, pp. 854–862, 2009.

[3] H. Irwin and A. Hurst, "Applications of geochemistry to sandstone reservoir studies," *Journal of the Geological Society*, vol. 12, pp. 127–146, 1983.

[4] J. Kantorowicz, "The nature, origin and distribution of authigenic clay minerals from Middle Jurassic Ravenscar and Brent Group sandstones.," *Clay Minerals*, vol. 19, no. 3, pp. 359–375, 1984.

[5] M. Lee, J. L. Aronson, and S. M. Savin, "Timing and conditions of Permian Rotliegende sandstone diagenesis, Southern North Sea: K/Ar and oxygen isotopic data," *The American Association of Petroleum Geologists Bulletin*, vol. 73, no. 2, pp. 195–215, 1989.

[6] C. I. Macaulay, A. E. Fallick, and R. S. Haszeldine, "Textural and isotopic variations in diagenetic kaolinite from the Magnus Oilfield sandstones," *Clay Minerals*, vol. 28, no. 4, pp. 625–639, 1993.

[7] G. E. McAulay, S. D. Burley, A. E. Fallick, and N. J. Kusznir, "Palaeohydrodynamic fluid flow regimes during diagenesis of the Brent Group in the Hutton-NW Hutton reservoirs: constraints from oxygen isotope studies of authigenic kaolin and reverse flexural modelling," *Clay Minerals*, vol. 29, no. 4, pp. 609–625, 1994.

[8] K. Purvis, "Diagenesis of Lower Jurassic sandstones, Block 211/13 (Penguin Area), UK northern North Sea," *Marine and Petroleum Geology*, vol. 12, no. 2, pp. 219–228, 1995.

[9] S. N. Ehrenberg, "Kaolinized, potassium-leached zones at the contacts of the Garn Formation, Haltenbanken, mid-Norwegian continental shelf," *Marine and Petroleum Geology*, vol. 8, no. 3, pp. 250–269, 1991.

[10] J. W. King and S. R. Austin, "Some characteristics of rolltype uranium deposits at gashills, wyoming," *U.S. Mining Engineers*, vol. 18, pp. 73–80, 1966.

[11] M. A. Chan, W. T. Parry, and J. R. Bowman, "Diagenetic hematite and manganese oxides and fault-related fluid flow in Jurassic sandstones, Southeastern Utah," *AAPG Bulletin*, vol. 84, no. 9, pp. 1281–1310, 2000.

[12] B. Beitler, M. A. Chan, and W. T. Parry, "Bleaching of Jurassic Navajo Sandstone on Colorado Plateau Laramide highs: Evidence of exhumed hydrocarbon supergiants?" *Geology*, vol. 31, no. 12, pp. 1041–1044, 2003.

[13] Y. P. Ma, C. Y. Liu, J. Q. Wang et al., "Effects of hydrocarbon migration and dissipation in later reformation of a basin: formation of Mesozoic bleached sandstone in northeastern Ordos basin," *Oil, Gas Geology*, vol. 27, Article ID 233240, pp. 233–240, 2006 (Chinese).

[14] M. J. Wilson, L. Wilson, and I. Patey, "The influence of individual clay minerals on formation damage of reservoir sandstones: A critical review with some new insights," *Clay Minerals*, vol. 49, no. 2, pp. 147–164, 2014.

[15] E. Harshman and S. Adams, "Geology and recognition criteria for roll-type uranium deposits in continental sandstones," Final Report, US Department of Energy & Grand Junction Office, 1980.

[16] R. H. DeVoto, "Uranium in Phanerozoic sandstone and volcanic rocks. Short course in uranium deposits; their mineralogy and origin," *Mineralogical Association of Canada*, vol. 3, pp. 293–305, 1978.

[17] B. Wu, A. Wei, C. Liu, Z. Song, L. Hu, and D. Wang, "Stable isotope tracing on the formation of white sandstone in Yan'an group, northern ordos basin, and its geological significance," *Earth Science Frontiers*, vol. 22, pp. 205–214, 2015 (Chinese).

[18] Z. Liu, S. Peng, M. Qin, H. Liu, S. Huang et al., "Multistage enrichment of the sawafuqi uranium deposit: new insights into sandstone-hosted uranium deposits in the intramontane basins of Tian Shan, China," *Acta Geologica Sinica*, vol. 91, no. 6, pp. 2138–2152, 2017.

[19] J. F. Davis, "Uranium in the USA: Genesis and Explorations," *Philosophical Transactions of the Royal Society of London. Series A, Mathematical and Physical Sciences*, vol. 206, no. 4416, pp. 298–306, 1979.

[20] S. Nakashima, J. R. Disnar, A. Perruchot, and J. Trichet, "Experimental study of mechanisms of fixation and reduction of uranium by sedimentary organic matter under diagenetic or hydrothermal conditions," *Geochimica et Cosmochimica Acta*, vol. 48, no. 11, pp. 2321–2329, 1984.

[21] C. S. Spirakis, "The roles of organic matter in the formation of uranium deposits in sedimentary rocks," *Ore Geology Reviews*, vol. 11, no. 1-3, pp. 53–69, 1996.

[22] J. P. McKinley, J. M. Zachara, S. C. Smith, and G. D. Turner, "The influence of uranyl hydrolysis and multiple site-binding reactions on adsorption of U(VI) to montmorillonite," *Clays and Clay Minerals*, vol. 43, no. 5, pp. 586–598, 1995.

[23] R. T. Pabalan and D. R. Turner, "Uranium(6+) sorption on montmorillonite: Experimental and surface complexation modeling study," *Aquatic Geochemistry*, vol. 2, no. 3, pp. 203–226, 1996.

[24] E. R. Sylwester, E. A. Hudson, and P. G. Allen, "The structure of uranium (VI) sorption complexes on silica, alumina, and montmorillonite," *Geochimica et Cosmochimica Acta*, vol. 64, no. 14, pp. 2431–2438, 2000.

[25] A. Kowal-Fouchard, R. Drot, E. Simoni, and J. J. Ehrhardt, "Use of spectroscopic techniques for uranium(VI)/montmorillonite interaction modeling," *Environmental Science & Technology*, vol. 38, no. 5, pp. 1399–1407, 2004.

[26] J. G. Catalano and G. E. Brown Jr., "Uranyl adsorption onto montmorillonite: Evaluation of binding sites and carbonate complexation," *Geochimica et Cosmochimica Acta*, vol. 69, no. 12, pp. 2995–3005, 2005.

[27] S. Bachmaf and B. J. Merkel, "Sorption of uranium(VI) at the clay mineral-water interface," *Environmental Earth Sciences*, vol. 63, no. 5, pp. 925–934, 2011.

[28] W. Dong, T. K. Tokunaga, J. A. Davis, and J. Wan, "Uranium(VI) adsorption and surface complexation modeling onto background sediments from the F-Area Savannah River site," *Environmental Science & Technology*, vol. 46, no. 3, pp. 1565–1571, 2012.

[29] M. Marques Fernandes, B. Baeyens, R. Dähn, A. C. Scheinost, and M. H. Bradbury, "U(VI) sorption on montmorillonite in the absence and presence of carbonate: A macroscopic and microscopic study," *Geochimica et Cosmochimica Acta*, vol. 93, pp. 262–277, 2012.

[30] M. Schindler, C. A. Legrand, and M. F. Hochella, "Alteration, adsorption and nucleation processes on clay-water interfaces: Mechanisms for the retention of uranium by altered clay surfaces on the nanometer scale," *Geochimica et Cosmochimica Acta*, vol. 153, pp. 15–36, 2015.

[31] OECD/NEA-IAEA, *Uranium 2007: Resources, Production and Demand, 2007 Red Book*, OECD, Paris, France, 2008.

[32] H. P. Taylor Jr., "The application of oxygen and hydrogen isotope studies to problems of hydrothermal alteration and ore deposition," *Economic Geology*, vol. 69, no. 6, pp. 843–883, 1974.

[33] B. Wang, L. S. Shu, D. Cluzel, M. Faure, and J. Charvet, "Geochemical constraints on Carboniferous volcanic rocks of the Yili Block (Xinjiang, NW China): Implication for the tectonic evolution of Western Tianshan," *Journal of Asian Earth Sciences*, vol. 29, no. 1, pp. 148–159, 2007.

[34] J. Charvet, L. Shu, S. Laurent-Charvet et al., "Palaeozoic tectonic evolution of the Tianshan belt, NW China," *Science China Earth Sciences*, vol. 54, no. 2, pp. 166–184, 2011.

[35] H. Liu, B. Wang, L. Shu, B.-M. Jahn, and Y. Lizuka, "Detrital zircon ages of Proterozoic meta-sedimentary rocks and Paleozoic sedimentary cover of the northern Yili Block: Implications for the tectonics of microcontinents in the Central Asian Orogenic Belt," *Precambrian Research*, vol. 252, pp. 209–222, 2014.

[36] HX. Liu, X. Zhang, B. Ding, and CY. Pan, "Metallogenic model and prospecting target of sandstone type uranium deposits in the southern Yili basin," *Uranium Geology*, vol. 31, Article ID 198205, pp. 198–205, 2015 (Chinese).

[37] D. M. Moore and R. C. Reynolds, *X–ray Diffraction and the Identification and Analysis of Clay Minerals*, Oxford University Press, London, UK, 1997.

[38] R. W. Potter II, M. A. Clynne, and D. L. Brown, "Freezing point depression of aqueous sodium chloride solutions," *Economic Geology*, vol. 73, no. 2, pp. 284-285, 1978.

[39] P. L. F. Collins, "Gas hydrates in CO_2-bearing fluid inclusions and the use of freezing data for estimation of salinity," *Economic Geology*, vol. 74, no. 6, pp. 1435–1444, 1979.

[40] D. L. Hall, S. M. Sterner, and R. J. Bodnar, "Freezing point depression of NaCl-KCl-H_2O solutions," *Economic Geology*, vol. 83, no. 1, pp. 197–202, 1988.

[41] R. J. Bodnar, "Revised equation and table for determining the freezing point depression of H2O-Nacl solutions," *Geochimica et Cosmochimica Acta*, vol. 57, no. 3, pp. 683-684, 1993.

[42] R. N. Clayton and T. K. Mayeda, "The use of bromine pentafluoride in the extraction of oxygen from oxides and silicates for isotopic analysis," *Geochimica et Cosmochimica Acta*, vol. 27, no. 1, pp. 43–52, 1963.

[43] R. H. Goldstein and T. J. Reynolds, "Systematics of fluid inclusions in diagenetic minerals: SEPM short course," *Society for Sedimentary Geology*, vol. 31, pp. 1–199, 1994.

[44] G. X. Chi and H. Z. Lu, "Validation and representation of fluid inclusion microthermometric data using the fluid inclusion assemblage (FIA) concept," *Acta Petrologica Sinica*, vol. 24, no. 9, pp. 1945–1953, 2008.

[45] G. Chi, T. Haid, D. Quirt, M. Fayek, N. Blamey, and H. Chu, "Petrography, fluid inclusion analysis, and geochronology of the End uranium deposit, Kiggavik, Nunavut, Canada," *Mineralium Deposita*, vol. 52, no. 2, pp. 1–22, 2016.

[46] E. Roedder, "Fluid inclusions," *Mineral Revolution*, vol. 12, pp. 1–646, 1984.

[47] S. M. Savin, "Oxygen and hydrogen isotope effects in low-temperature mineral-water interaction," in *Handbook of Environmental Isotope Geochemistry*, P. Fritz and J. Ch. Fontes, Eds., Elsevier, 1980.

[48] J. X. Dai, X. G. Pei, and H. F. Qi, *China Natural Gas Geology*, vol. 1, Petroleum Industry Press, Beijing, China, 1992.

[49] B. Wu, C. Liu, and J. Wang, "Basical characteristics of fluid geologic process of interlayer oxidation zone sandstone-type uranium deposit," *Science China Earth Sciences*, vol. 50, no. 2, pp. 185–194, 2007.

[50] R. J. Bodnar, "Philosophy of fluid inclusion analysis," in *Fluid inclusions in minerals, Methods and Applications*, B. De Vivo and M. L. Frezzotti, Eds., Virginia Tech, Blacksburg, 1994.

[51] G. W. Brindley, C. C. Kao, J. L. Harrison, M. Lipsicas, and R. Raythatha, "Relation between structural disorder and other characteristics of kaolinites and dickites.," *Clays and Clay Minerals*, vol. 34, no. 3, pp. 239–249, 1986.

[52] B. Lanson, D. Beaufort, G. Berger, A. Bauer, A. Cassagnabère, and A. Meunier, "Authigenic kaolin and illitic minerals during burial diagenesis of sandstones: a review," *Clay Minerals*, vol. 37, no. 1, pp. 1–22, 2002.

[53] R. C. Tobin, "Diagenesis, thermal maturation and burial history of the Upper Cambrian Bonneterre dolomite, southeastern Missouri; an interpretation of thermal history from petrographic and fluid inclusion evidence," *Organic Geochemistry*, vol. 17, no. 2, pp. 143–151, 1991.

[54] R. C. Surdam, L. J. Crossey, E. S. Hagen, and H. P. Heasler, "Organicinorganic interaction and sandstone diagwenesis," *AAPG Bulletin*, vol. 78, pp. 1–23, 1989.

[55] R. C. Surdam, Z. S. Jiao, and D. B. MacGowen, "Redox reactions involving hydrocarbons and mineral oxidants: a mechanism for significant porosity enhancement in sandstones," *AAPG Bulletin*, vol. 77, pp. 1509–1518, 1993.

[56] L. Yang, T. Xu, K. Liu, B. Peng, Z. Yu, and X. Xu, "Fluid–rock interactions during continuous diagenesis of sandstone reservoirs and their effects on reservoir porosity," *Sedimentology*, vol. 64, no. 5, pp. 1303–1321, 2017.

[57] J. A. Cartwright, "Episodic basin-wide fluid expulsion from geopressured shale sequences in the North Sea Basin," *Geology*, vol. 22, no. 5, pp. 447–450, 1994.

[58] C. Xue, G. Chi, and W. Xue, "Interaction of two fluid systems in the formation of sandstone-hosted uranium deposits in the Ordos Basin: geochemical evidence and hydrodynamic modeling," *Journal of Geochemical Exploration*, vol. 106, no. 1-3, pp. 226–235, 2010.

[59] M. S. Hendrix, T. A. Dumitru, and S. A. Graham, "Late Oligocene-early Miocene unroofing in the chinese Tian Shan: an early effect of the India-Asia collision," *Geology*, vol. 22, no. 6, pp. 487–490, 1994.

[60] M. E. Bullen, D. W. Burbank, J. I. Garver, and K. Y. Abdrakhmatov, "Late cenozoic tectonic evolution of the northwestern tien shan: new age estimates for the initiation of mountain building," *Bulletin of the Geological Society of America*, vol. 113, no. 12, pp. 1544–1559, 2001.

[61] M. Person and G. Garven, "A sensitivity study of the driving forces on fluid flow during continental-rift basin evolution," *Geological Society of America Bulletin*, vol. 106, no. 4, pp. 461–475, 1994.

[62] P. Landais, "Organic geochemistry of sedimentary uranium ore deposits," *Ore Geology Reviews*, vol. 11, no. 1-3, pp. 33–51, 1996.

[63] S. A. Wood, "The role of humic substances in the transport and fixation of metals of economic interest (Au, Pt, Pd, U, V)," *Ore Geology Reviews*, vol. 11, no. 1-3, pp. 1–31, 1996.

[64] D. J. Mossman, F. Gauthier-Lafaye, and S. E. Jackson, "Black shales, organic matter, ore genesis and hydrocarbon generation in the Paleoproterozoic Franceville Series, Gabon," *Precambrian Research*, vol. 137, no. 3-4, pp. 253–272, 2005.

[65] B. Smieja-Król, S. Duber, and J.-N. Rouzaud, "Multiscale organisation of organic matter associated with gold and uranium minerals in the Witwatersrand basin, South Africa," *International Journal of Coal Geology*, vol. 78, no. 1, pp. 77–88, 2009.

[66] S. Fuchs, D. Schumann, A. E. Williams-Jones, and H. Vali, "The growth and concentration of uranium and titanium minerals in hydrocarbons of the carbon leader reef, witwatersrand supergroup, South Africa," *Chemical Geology*, vol. 393-394, pp. 55–66, 2015.